Characterization and Improvement of Infra-Red Video Bolometry Camera and Codes for NSTX-U

Rian Chandra[1], Matt Reinke[2], Byron Peterson[3], G. G. Van Eden[4], Ryuchi Sano[5]

[1](University of Washington), [2](ORNL), [3](Nat. Ins. Fus. Sci, JP) , [4](DIFFER, NL), [5](Nat. Inst. Quant. Rad. Sci. Tech., JP)

DIFFER Dutch Institute for Fundamental Energy Research | Oak Ridge National Laboratory | U.S. Department of Energy | PPPL PRINCETON PLASMA PHYSICS LABORATORY

Objectives:

- **Design a single channel, 0-D IR Photoconductive Bolometry system.**
- **Build and test this system, compare performance to the 2-D IRVB to determine feasibility.**
- **Vectorize aspects of the IRVB analysis code to improve performance.**
- **Characterize the performance of several IRVB cameras, across a range of operating parameters and processing methods.**
- **Explore why the codes do not correctly return input calibration values.**

Overview of Infra-Red Photoconductive Bolometer (IRPB)

A. The plasma, which looses energy though radiation.
B. A 2.5μm Pt foil absorbs this energy, and heats up.
C. IR light from the foil is focused by a CaF_2 lens.
D. A Photoconductive sensor measures this IR power.

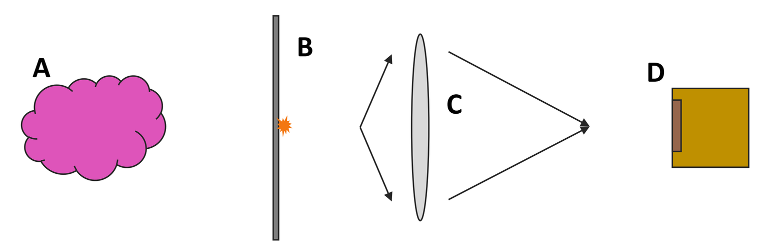

Figure 1: Hardware Schematic of the IRPB Setup

Mathematical Description of the IRPB

The temperature rise of the foil can be estimated from the input power as follows:

$$T_{Foil} = \frac{P_{in} \times \tau \times A_{Foil}}{\rho c_p V_{Foil}} \quad [^oK] \quad (1)$$

Where the thermal time constant $\tau = \frac{A_{Foil}}{\kappa}$ and the volume $V_{Foil} = t_{Foil} A_{Foil}$, for thermal diffusivity $\kappa = .26 \; [cm^2/s]$, Density $\rho = 21{,}500 \; [kg/m^3]$, Heat capacity $c_p = .133 \; [J/g * K]$, $t_{Foil} = 2.5\mu m$.

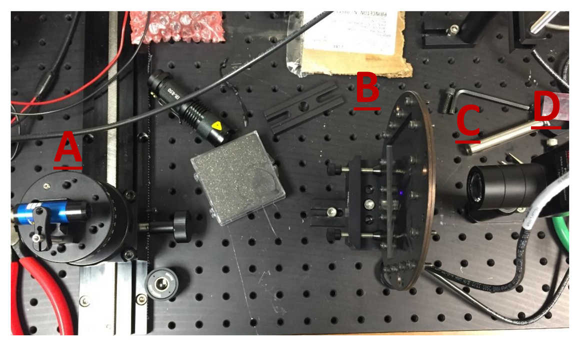

Figure 2: Physical IRPB benchtop setup, with laser. Letters correspond with Fig. 1, Laser mimics plasma

The power emitted by the foil (the luminance) due to this temperature rise can be calculated using the Planck blackbody distribution:

$$L_{Foil} = \frac{(\epsilon) 2hc^2}{\lambda^5} \frac{1}{e^{\frac{hc}{\lambda T k_b}} - 1} \quad [W/Area * \Omega * \lambda] \quad (2)$$

From this, we can calculate the signal output by the detector:

$$V_{out} = \left(\frac{2\pi A_{Foil}}{16}\right) \times (\epsilon) \times \int_{\Delta\lambda} \mathcal{R} \times L_{Foil}\Big|_{T_{Foil}} d\lambda \quad [V] \quad (3)$$

Where the first term is the etendu of the light collected by the lens, ϵ is the emissivity of the foil in the IR range ($\cong$.83), the luminance is evaluated at the foil temperature of interest, $\mathcal{R}$ is the detector responsivity (in V/W) and the integral is taken over the sensitive range of the detector. Without the responsivity term, this integral would give the detector flux ψ_{Det}.

Predictive Results:

We evaluate V_{out} over a range of input power, and use least-squares minimization to find P_{in} such that $V_{out} - V_{background}$ equals the detector noise voltage (the Noise-Equivalent-Power-Density, NEPD). Giving the foil an offset temperature was found to drop the SNR as well, but was not pursued further.

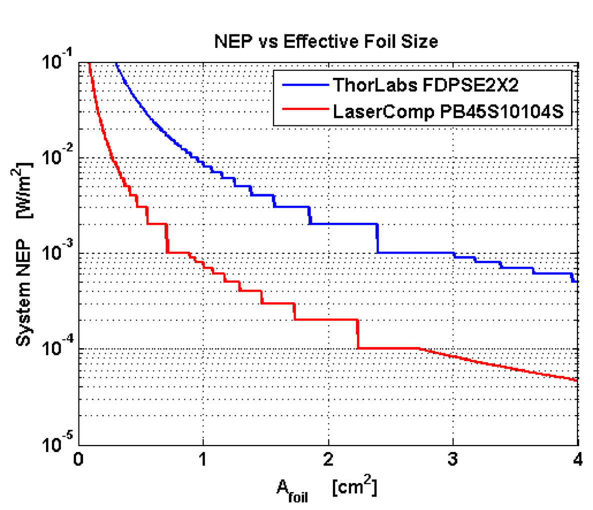

Figure 3: NEPD vs Focused Foil Area, for ThorLabs and LaserComponents sensors

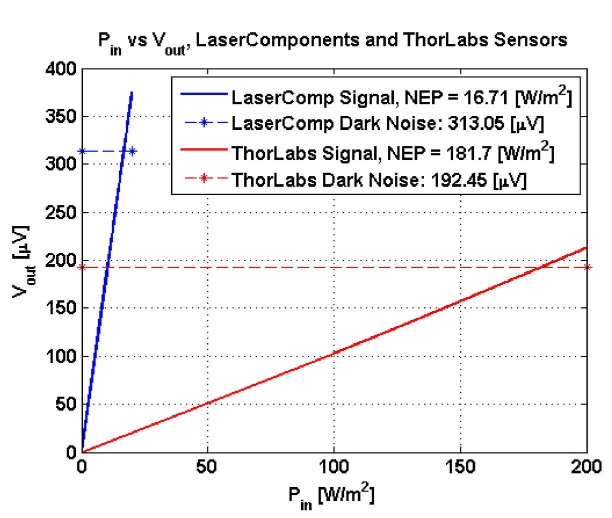

Figure 4: IRPB Predicted NEPD, A_{det}=4mm^2, 200kHz, ThorLabs FDPSE2X2 sensor, LaserComponents PB45S10104S.

Experimental Data and Analysis:

Data was collected using a 5mW laser over approximately a 4mm^2 spot on the foil described above, using the ThorLabs FDPSE2X2 detector ($\lambda \approx .5 - 1.3\mu m$). Figure 6 plots the raw data, with a signal-to-noise ratio (SNR) of 2.66, and the 1kHz resampled data, with an SNR of 7.52. The next stage is to compute the power from the raw signal, using the first order, 0-D "τ-derivative":

$$P_{out} = \alpha \times [S_{raw} + \tau \times \frac{dS}{dt}] \quad [W/m^2] \quad (4)$$

Where τ is the thermal time constant, calibrated to recover the input square wave shape, and α is a calibrated scaling factor to convert the signal to power density.

The resulting signal appears to return the characteristic laser square wave better than the raw data, but even downsampled to 20Hz, the SNR remains 2.6 (Fig. 5).

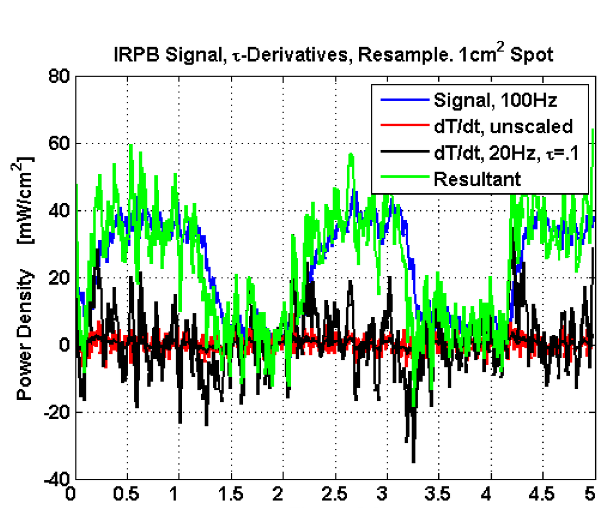

Figure 5: IRPB derivative terms and weighting. No α calibrated conversion to power density is applied.

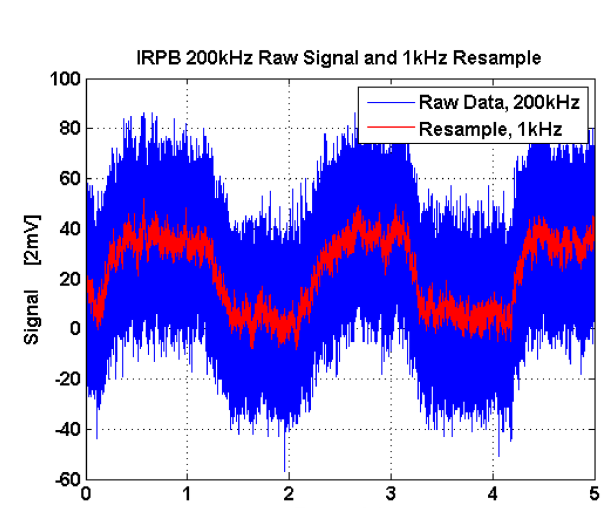

Figure 6: IRPB Raw Signal and 200kHz downsampled signal.

Overview of the Infra-Red Video Bolometer (IRVB)

The hardware system of the IRVB is almost identical to the IRPB, with the replacement of the optical lens for the camera lens, and the photoconductive sensor for an array of sensors. The vacuum hardware and progression of the data from the physical foil, to the thermal view of the foil, to the region of interest is shown right.

Three cameras (FLIR A655sc and A6751, and Santa-Barbra Focal Plane (SBFP)) were calibrated by heating the Pt foil (pictured right) with a 5mW "BlueLyte" diode laser laser over a specified range of power (by adjusting the input voltage from 0.0 to 1.3V) and frequency, to interrogate relivant plasma powers and timescales, respectively. A frame before and after the laser is turned off is pictured in Fig. 12.

The power is calculated using Eq. 5. The individual derivative terms and raw temperature rise are averaged over a portion of the laser spot and given in Fig. 12,13. The utility of both derivative terms should be clear from this figure.

Unfortunately, the measured power does not match the power of the calibration laser as measured directly by an IR silicon photodiode. The degree of mismatch α is plotted right (Fig. 10). The remainder of this project was dedicated to understanding and correcting this discrepancy.

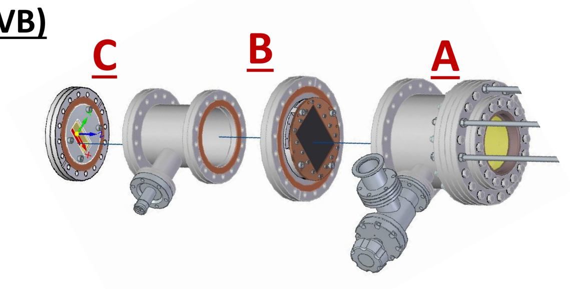

Figure 7: SBFP installed on NSTX-U upper bay H. A: Camera support. B: Foil. C: Aperture to plasma

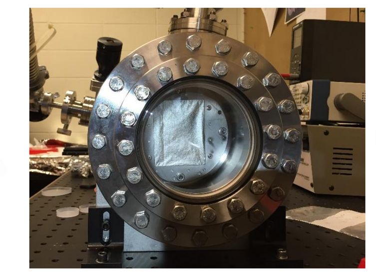

Figure 8: Partial camera view of blackened Pt foil through IR window

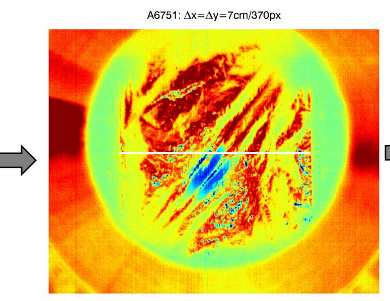

Figure 9: A6751 Foil view and length

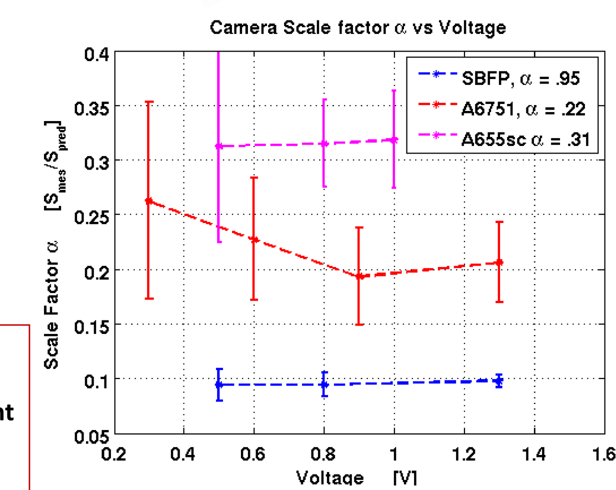

Figure 10: Scale factor α between measured and predicted power densities, all cameras

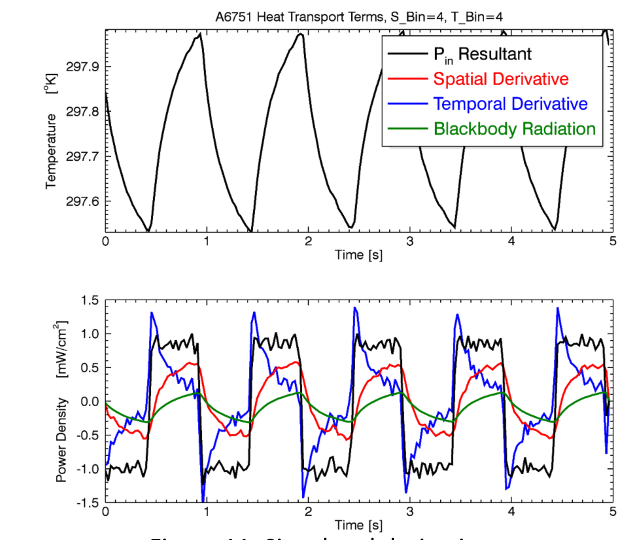

Figure 11: Signal and derivative terms over fraction of laser spot, A6751 1.3V

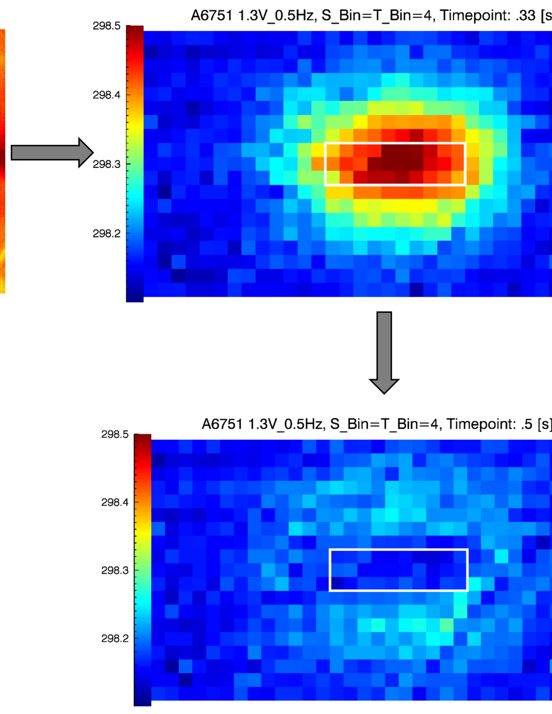

Figure 12,13: Background subtracted region around laser spot, before and after the laser turns off. White square is 7.5x2.75mm^2 region of laser spot. Characteristic "ring" in lower figure is heat diffusing away.

Further Investigation

To find the cause of this largely linear discrepancy between predicted and measured powers, we examined binning the data in space and time before processing, moving the output averaging area, modifying the counts to temperature gain, and changing foil parameters.

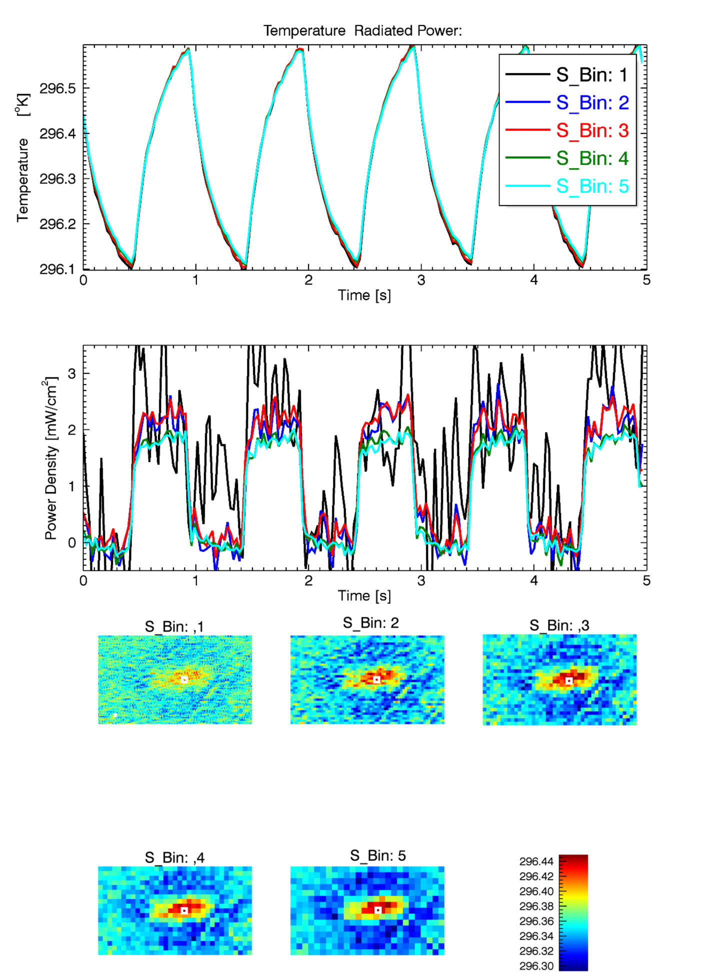

Figure 17,18: Spatial Binning Study. White square is the 2x2mm^2 averaging area inside the laser spot. Binning occurs before derivatives are taken, decreases noise.

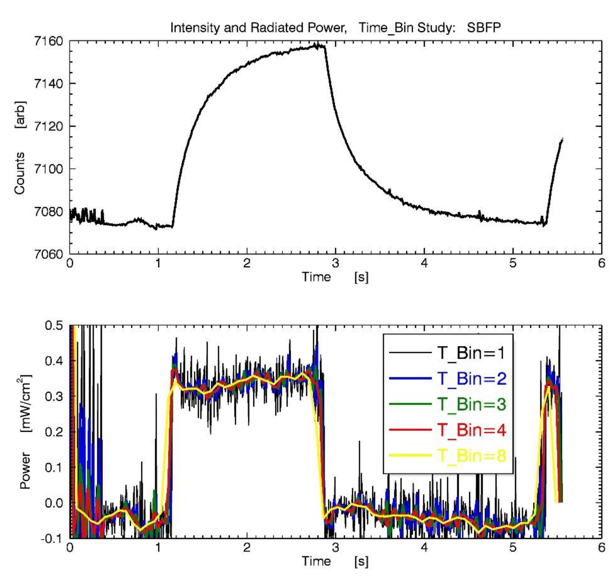

Figure 14: Time Binning Study. Frames are averaged before derivatives are taken, noise decreases predictably. SBFP 1.3V, 0.2Hz data set.

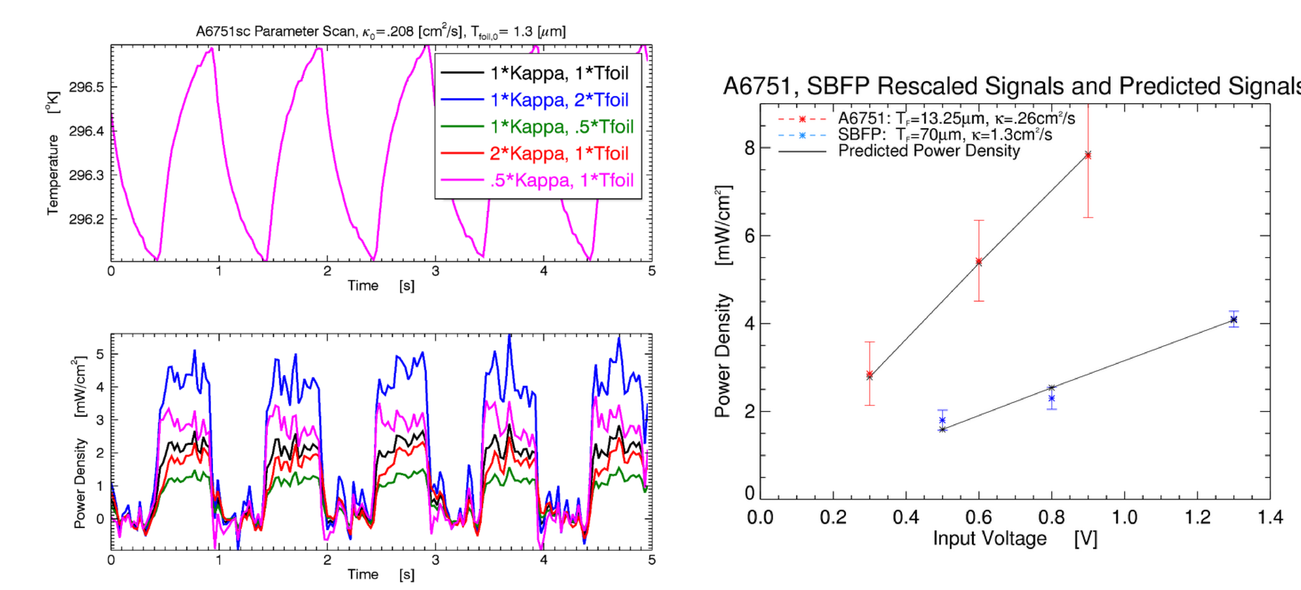

Figure 15,16: Scaling physical foil parameters, A6751 0.9V, 0.2Hz dataset. Note the changes in characteristic shape. Changing t_f and κ can correct the SBFP and A6751 power scan while preserving shape, but are both unphysically high

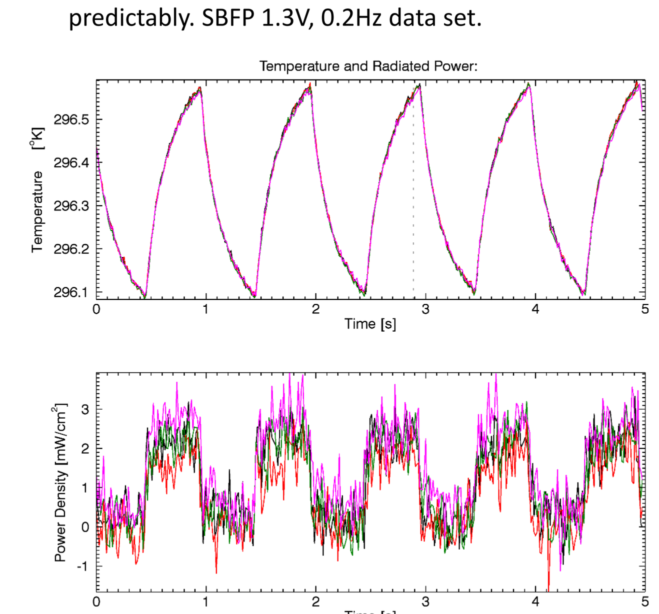

Figure 19: Averaging power over a 2x2mm^2 spot, moved to four positions in a 4x4mm^2 grid inside the laser spot, A6571 1.3V 0.9Hz. No space or time binning. Signal is stable

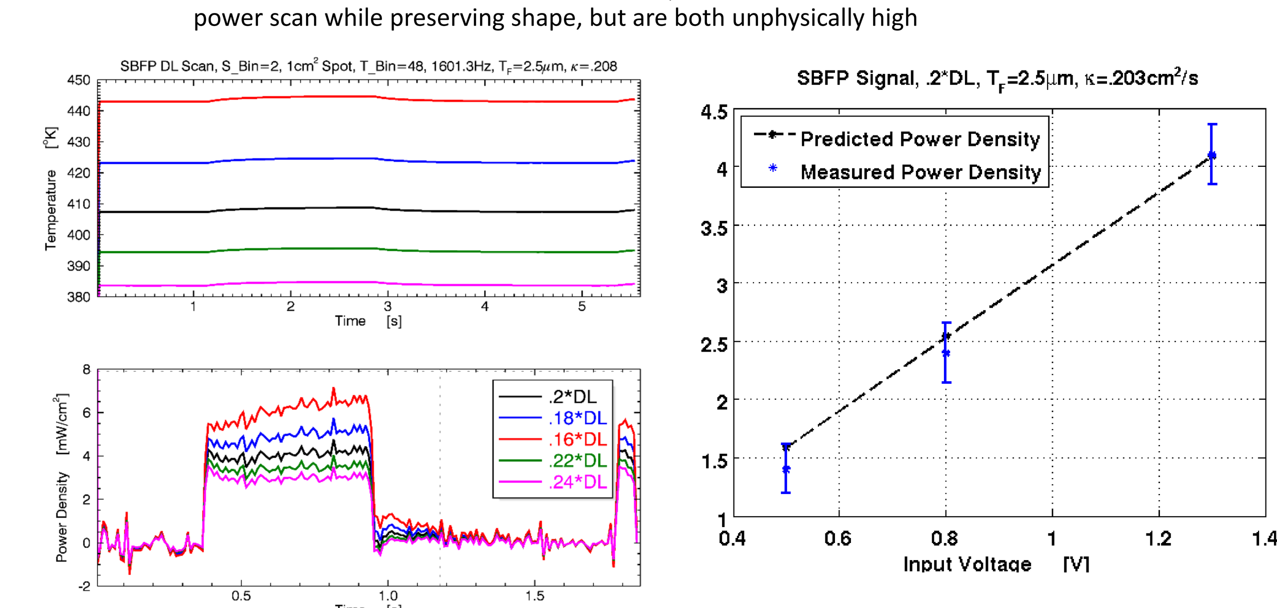

Figure 20,21: Scaling the SBFP counts-to-temperature conversion factor "DL" to match predicted power. .2DL corrects the power scan, but implies that the blackbody calibration source was 2.24 times too close to the camera, and gives unphysical offset.

Results and Comparisons

Despite the inability to reproduce the expected input power in magnitude, we can still examine the relative scaling in input power and frequency. Previous work has looked at this for the purpose of predicting signal to noise ratio, and NEP, but only with the raw signal. Here, we extend this to an analysis of the τ-derivative scheme (Eq. 4), and the full spatio-temporal derivative scheme (Eq. 5).

For full generalization, we report the "Sensor NEPD", normalized by $\sqrt{A_{det}}\sqrt{t_{res}}$ for the correct scaling.

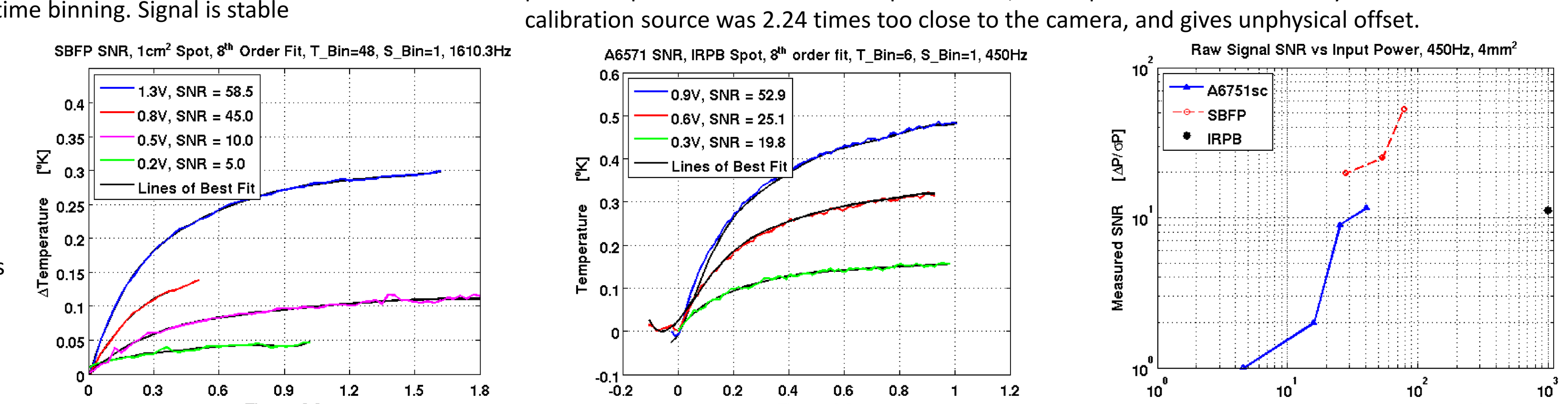

Figures 22,23,24: Noise, calculated by subtracting an 8th order polynomial fit from the signal, and SNR normalized by $\sqrt{A_{det}}\sqrt{t_{res}}$ to 450Hz, 4mm^2, as in SNEPD.

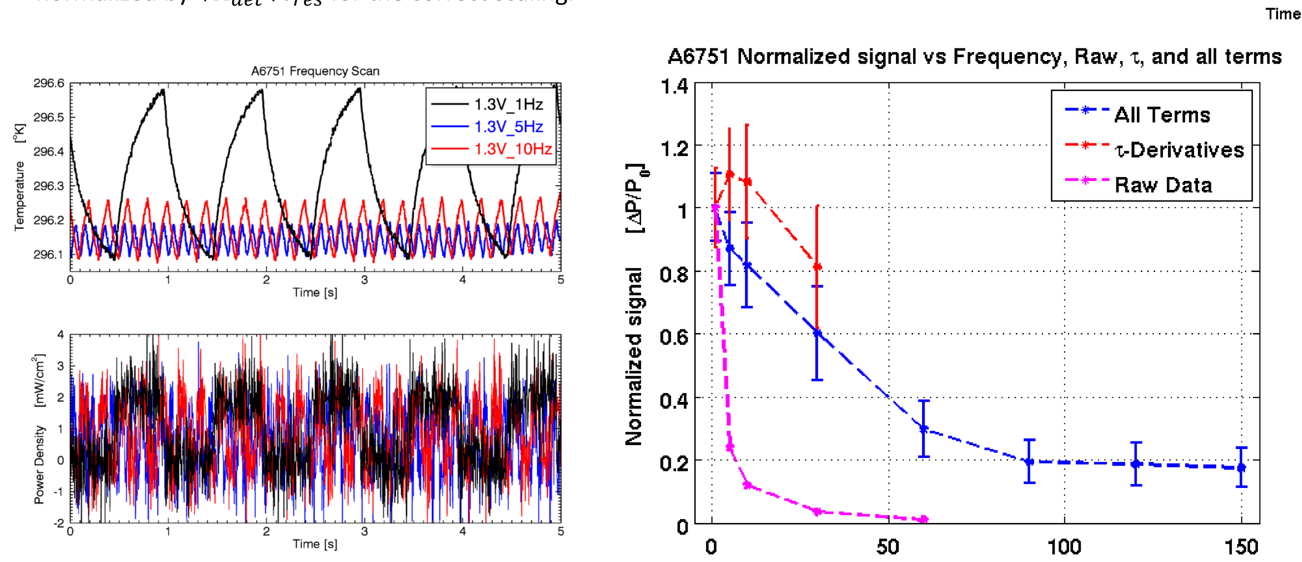

Figure 25,26: A6751 Frequency Scan raw data and full derivatives (T_bin=S_bin=1), and comparison plot including τ-derivatives. The raw vs full terms dynamics are clearly visible in the data.

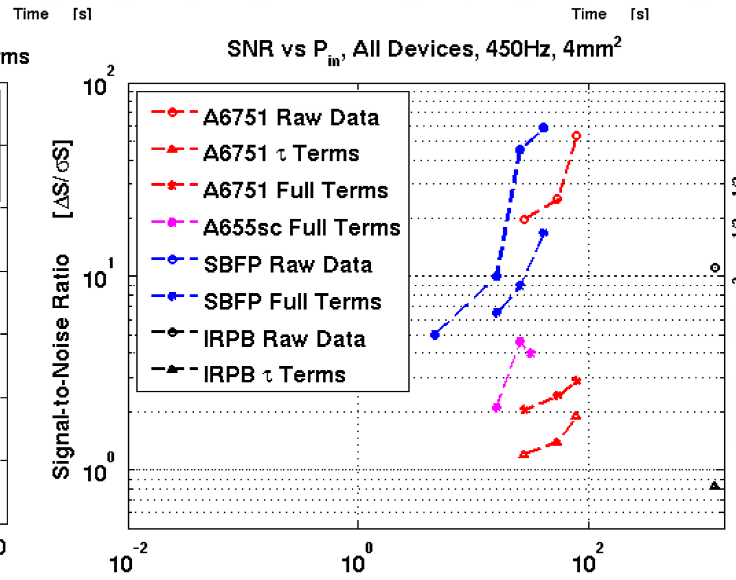

Figure 27: SNR vs Voltage, all cameras, IRPB measured values.

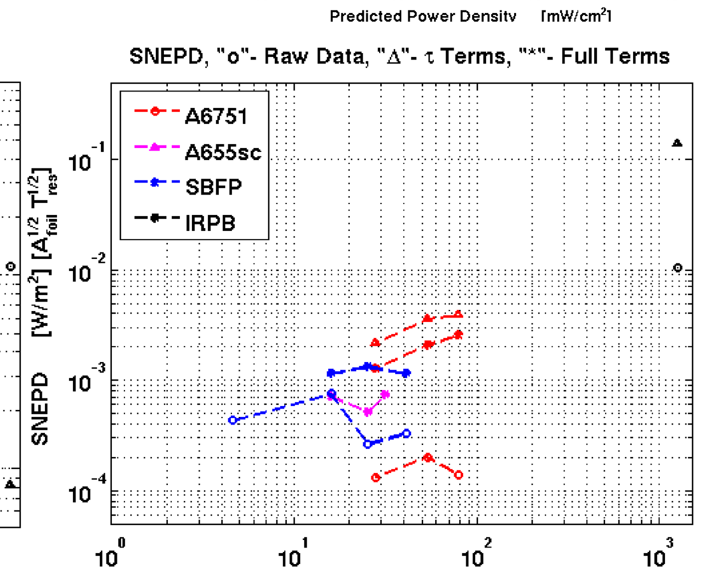

Figure 28: SNEPD, all cameras, IRPB measured values.

Mathematics of the IRVB

The relationship between the observed temperature and the input power is governed by the 2D heat transport equation:

$$\Omega_{rad} = \frac{1}{\kappa}\frac{\partial T}{\partial t} - \left[\frac{\partial^2 T}{\partial x^2} + \frac{\partial^2 T}{\partial y^2}\right] + \Omega_{bb} \quad [K/m^2] \quad (5)$$

Where Ω_{rad} is the radiated power onto the foil, Ω_{bb} is the blackbody power, and κ is the thermal diffusivity (sometimes labeled α). We further expand:

$$\Omega_{rad} = \frac{P_{rad}}{k t_F A_F} \qquad \Omega_{bb} = \frac{(\epsilon)\sigma_{SB}(T^4 - T_0^4)}{k t_F} \quad (6)$$

Where k is the thermal conductivity, ϵ is the foil emissivity, σ_{SB} is the Stephan-Boltzman constant, and T_0 is the background temperature.

This PDE is solved numerically through the Crank-Nicholson discretization, in which the temporal and spatial derivatives are approximated by first order, first and second centered difference schemes, respectively. The time and x- derivatives are given below (y can be inferred):

$$T_t(x_i, y_j, t_{n+1/2}) \approx \frac{T(x_i, y_j, t_{n+1}) - T(x_i, y_j, t_n)}{\Delta t} \quad \left[\frac{K}{s}\right] \quad (7)$$

$$T_{xx}\left(x_i, y_j, t_{n+\frac{1}{2}}\right) \approx \ldots$$

$$\frac{1}{2}\left[\frac{T(x_{i-1}, y_j, t_{n+1}) - 2T(x_i, y_j, t_{n+1}) + T(x_{i-1}, y_j, t_{n+1})}{(\Delta x)^2} + \ldots \frac{T(x_{i-1}, y_j, t_n) - 2T(x_i, y_j, t_n) + T(x_{i-1}, y_j, t_n)}{(\Delta x)^2}\right] \quad \left[\frac{K}{m^2}\right] \quad (8)$$

Vectorization:

Traditionally, the Crank-Nicholson scheme would be implemented iteratively for each pixel in a 2D region of the CCD, for each frame (with a padded border set to the background temperature). However, this is highly memory inefficient. Instead, we have vectorized this process, and others in the code, to achieve significant increases in speed, making the code deployable on an inter-shot timescale.

This process can be conceptualized for the time derivative term as follows: Consider the temperature data as a matrix of frames over time. By subtracting the submatrix of frames 0→n-1 from the submatrix of frames 1→n, we form the time derivative matrix for all pixels.

$$\begin{array}{|c|c|c|c|}\hline \frac{\partial T(x_i, y_j, t_o)}{\partial t} & \frac{\partial T(x_i, y_j, t_1)}{\partial t} & \ldots & \frac{\partial T(x_i, y_j, t_{n-1})}{\partial t} \\ \hline \end{array}$$

$$=$$

$$\begin{array}{|c|c|c|c|c|}\hline T(x_i, y_j, t_o) & T(x_i, y_j, t_1) & \ldots & T(x_i, y_j, t_{n-1}) & T(x_i, y_j, t_n) \\ \hline \end{array}$$

$$-$$

$$\begin{array}{|c|c|c|c|c|}\hline T(x_i, y_j, t_o) & T(x_i, y_j, t_1) & \ldots & T(x_i, y_j, t_{n-1}) & T(x_i, y_j, t_n) \\ \hline \end{array}$$

Figure 29: One pixel's time derivative, conceptualized as offset time history subvectors

Similar ideas have been applied to the Spatial derivative, SBFP conversion to temperature, and the SBFP video file decompression.

Operation:	UnVectorized: [S]/[# points]	Vectorized: [S]/[# points]
Derivatives:	2.35/413070	0.035/413070
SBFP Gain:	0.539/54600	0.006/54600
Decompression:	13.88/1.33E6	1.2/1.33E6

Table 1: Computational time gains with vectorization

Conclusions:

- The IRVB analysis codes, ran on calibration data, report an input power which differs from the known value by a constant, unique to each camera (Fig. 10).
  - We find that the foil thickness, thermal diffusivity, and SBFP counts-to-temperature gain all could explain this discrepancy, but only if they are set unphysically high (Fig. 15,6 and 20,21).
  - Further tests included re-checking the foil reflectivity ($\approx$3%),and thickness ($\approx$3μm).
- We find that the raw data has the best SNR, followed by the 2D, then 0D derivatives, and that the SNR decreases with input power, as expected (Fig. 27).
- We find that the signal amplitude decreases fastest with frequency in the raw data, followed by the 2D and 0D derivatives (Fig 25,26).
- An IR Photoconductive Bolometer was tested, and found to have worse SNR than the IRVBs in raw data and 0D derivatives, but may have lower cost per channel, if pixel binning is accounted for. The LaserComponents sensor may improved SNR (Fig. 5)
- The "SNEPD" figure-of-merit is developed to generalize the NEPD for spatial averaging. It is (relatively) stable across a range of input power density (Fig. 28).
- Vectorization of the derivatives for all cameras, and temperature conversion, decompression for the SBFP allows for inter-shot processing timescales (Tbl. 1).
- **Future work will collect further benchtop data with the camera removed from the machine to correct the observed discrepancies, before the IRVB is fully deployed on NSTX-U in F.Y. '17.**

References and Acknowledgements:

1) Design and characterization of a prototype divertor viewing infrared video bolometer for NSTX-U, van Eden, G. G. et. Al., Rev. Sci. Instrum., 87, 11D402 (2016)
2) In situ calibration of an infrared imaging video bolometer in the Large Helical Device, Mukai, K. et. Al, Rev. Sci. Instrum., 85, 11E435 (2014)
3) Development of imaging bolometers for magnetic fusion reactors (invited), Peterson, Byron J. Et Al, Rev. Sci. Instrum., 79, 10E301 (2008)

- The author would like to acknowledge Dr. Matt Reinke, and the SULI program coordinators.
- This work was made possible by funding from the Department of Energy for the Summer Undergraduate Laboratory Internship (SULI) program. This work is supported by the US DOE Contract No. DE-AC02-09CH11466.